iScience

CellPress
OPEN ACCESS

Article

Fasnall Induces Atypically Transient Stress Granules Independently of FASN Inhibition

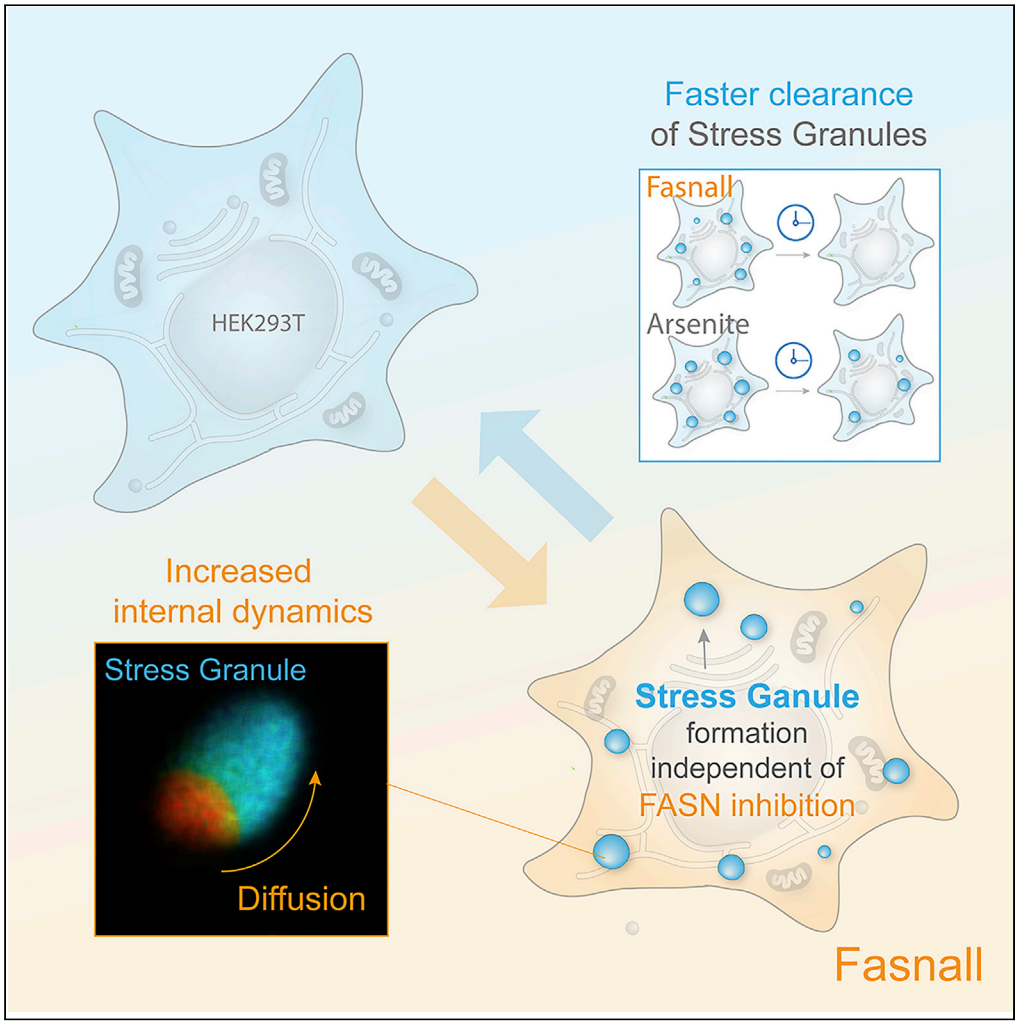

Triana Amen,
Daniel Kaganovich

daniel.kaganovich@med.uni-goettingen.de

HIGHLIGHTS

Stress Granules can have different physical properties and clearance rates

Fasnall induces Stress Granule formation

Fasnall-induced Stress Granules have increased dynamics

Fasnall-induced Stress Granules form independently of FASN inhibition

Amen & Kaganovich, iScience *23*, 101550
October 23, 2020
https://doi.org/10.1016/j.isci.2020.101550

iScience

CellPress
OPEN ACCESS

Article

Fasnall Induces Atypically Transient Stress Granules Independently of FASN Inhibition

Triana Amen[1] and Daniel Kaganovich[1,2,3,*]

SUMMARY

Stress Granule formation has been linked to the resistance of some cancer cells to chemotherapeutic intervention. A number of studies have proposed that certain anti-tumor compounds promote cancer cell survival by inducing Stress Granule formation, leading to increased cellular fitness and apoptosis avoidance. Here we show that a potent fatty acid synthase inhibitor, fasnall, known for its anti-tumor capabilities, triggers the formation of atypical Stress Granules, independently of fatty acid synthase inhibition, characterized by high internal mobility and rapid turnover.

INTRODUCTION

Stress Granules (SGs) are membraneless ribonucleoprotein compartments that form transiently during stress in most cell types ranging from yeast and plants to mammals (Kedersha and Anderson, 2002; Buchan et al., 2011; Buchan and Parker, 2009). SGs contain stalled pre-initiation complexes and RNA-binding proteins, such as TDP43, FUS, and kinases (Protter and Parker, 2016; Buchan and Parker, 2009; Walker et al., 2013; Lenzi et al., 2015). Among their many proposed functions, they are thought to serve as signaling hubs during stress conditions, regulating apoptosis, production of reactive oxygen species, nucleocytoplasmic transport, kinase signaling, and other vital cellular functions (Buchan and Parker, 2009; Kedersha and Anderson, 2007; Takahara and Maeda, 2012; Arimoto et al., 2008; Takahashi et al., 2013; Zhang et al., 2018; Thedieck et al., 2013; Amen and Kaganovich, 2020; Kaganovich, 2017). Indeed, key signaling factors, like protein kinase C, and mTORC1 components localize to SGs (Amen and Kaganovich, 2020; Fournier et al., 2013; Jevtov et al., 2015; Sfakianos et al., 2018; Thedieck et al., 2013; Kobayashi et al., 2012). SG formation and composition are fine-tuned in accordance with the specific type of stress (Aditi Mason et al., 2019; Heberle et al., 2019; Jevtov et al., 2015; Kobayashi et al., 2012; Buchan et al., 2011). It is becoming increasingly clear that precise regulation of SG composition and physical properties is critical for its cellular function (Dewey et al., 2012; Mateju et al., 2017; Patel et al., 2015; Aulas et al., 2017). For example, aberrant aggregation in SGs is implicated in the cellular pathology of amyotrophic lateral sclerosis, an age-related neurodegenerative disorder (Patel et al., 2015; Li et al., 2013; Wolozin and Ivanov, 2019).

Recent work has identified an important role for SGs in cancer. SGs incorporate multiple proteins involved in tumorogenesis, and SG components are often aberrantly expressed or mutated in cancers (Choi et al., 2019; Protter and Parker, 2016). In addition, chemotherapeutic drugs, such as bortezomib, lapatinib, and 5-fluorouracil, have been shown to induce SG formation (Adjibade et al., 2020; Kaehler et al., 2014; Anderson et al., 2015; Fournier et al., 2010). Furthermore, a link between cancer progression and SG formation is beginning to emerge. For example, several important studies have shown that SG formation promotes cancer cell survival (Choi et al., 2019; El-Naggar and Sorensen, 2018). In particular, SGs have been shown to increase cellular fitness in KRAS cancer cell lines, possibly also protecting cells from chemotherapeutic interventions (Grabocka and Bar-Sagi, 2016; Anderson et al., 2015). SGs have also been shown to protect cells from apoptosis, reducing the amount of reactive oxygen species (Thedieck et al., 2013; Takahashi et al., 2013). Inhibition of SG formation sensitizes cancer cells to anti-tumor drugs (Timalsina et al., 2018). Important questions, however, remain unanswered. It is not clear, for instance, how SG-associated downregulation of mTORC1 activity and the subsequent reduction in protein biosynthesis can be reconciled with other hallmarks of cancer, such as evading growth suppression, hyperactive proliferation, and abundant protein synthesis (Anderson et al., 2015). On the other hand, some conditions, such as selenite treatment, lead to

[1]Department of Experimental Neurodegeneration, University Medical Center Goettingen, 37073 Goettingen, Germany

[2]1Base Pharmaceuticals, Boston, MA 02129, USA

[3]Lead Contact

*Correspondence: daniel.kaganovich@med.uni-goettingen.de

https://doi.org/10.1016/j.isci.2020.101550

the formation of "non-canonical" SGs with pro-apoptotic effects due to a translation block initiated from eIF4F complex formation inhibition (Fujimura et al., 2012). Other small molecules that inhibit translation initiation through eIF4A-eIF4F assembly, including pateamine A, silvestrol, and hippuristanol, also induce "non-canonical" SG assembly and have similar pro-apoptotic effects on cancer cells (Bordeleau et al., 2006; Low et al., 2005; Cencic and Pelletier, 2016; Chen et al., 2016; Kogure et al., 2013; Patton et al., 2015; Dang et al., 2006; Slaine et al., 2017; Mazroui et al., 2006). Therefore, to develop a clear understanding of the mode of action of SG, it is important to identify the trigger-specific differences in their assembly, dynamics, and composition.

Our data identify an anti-tumor compound that triggers SG formation. We show that a potent fatty acid synthase (FASN) inhibitor and anti-tumor reagent (Alwarawrah et al., 2016), fasnall, induces SG formation in human cells. We demonstrate that fasnall-induced SGs have higher internal dynamics, faster clearance kinetics, and slightly different composition than SGs induced by arsenite treatment. Finally, we show that fasnall induces SG formation independently of its FASN inhibition activity.

RESULTS

Fasnall Induces Stress Granule Formation

We identified fasnall in the screen for PABPC1 inclusion formation. PABPC1 is a major component of SGs (Aulas et al., 2017; Jain et al., 2016), thus we set out to determine whether these granules are, in fact, SGs. First, we confirmed that PABPC1-positive inclusions harbor other SG markers, G3BP and TIA1, by immunofluorescence in the endogenously tagged PABPC1 human cell line, and in an independent cell line without fluorescent tags (Figures 1A and S1A). The timeline of SG formation was similar to that of arsenite-induced SGs (Figure 1B), with the majority of HEK293T cells forming SGs after 1 h of treatment (Figure 1B). However, SG formation was delayed in HeLa cells (Figure S1B) and the clearance time was markedly different. Fasnall-induced SGs cleared in 15 min, whereas arsenite-induced SGs needed almost 4 times as much time to clear (Figures 1C and S1C) (Wheeler et al., 2016). However, both arsenite and fasnall-induced SGs exhibited a slight increase in size at the beginning of the recovery (Figures 1C and S1F). Inhibition of polysome disassembly by cycloheximide is known to inhibit SG formation (Mollet et al., 2008), and addition of cycloheximide to fasnall prevented SG formation as well (Figures 1D and S1G). Next, we assessed eIF2 phosphorylation at the Ser51, a marker for arsenite-induced SGs (Rabouw et al., 2020). Fasnall did not induce phosphorylation, as opposed to arsenite treatment (Figures 1E and S2A). Not surprisingly, fasnall also did not induce a significant reduction in the translation (Figure 1F), as assessed by FAM-dC-puromycin incorporation (Starck et al., 2004).

SGs are multiprotein granules that potentially consist of over a hundred different proteins (Jain et al., 2016). We asked whether the SG proteome in fasnall conditions is similar to the proteome of SGs that form in response to arsenite treatment, a commonly used SG trigger (Lu et al., 2001) (Figure 1G). This was done using the proteomic BioID approach (Roux et al., 2013), which entailed expressing PABPC1-BirA (R118G)-GFP resulting in proximity-associated biotinylation of PABPC1-interacting proteins, and subsequent subtraction of control condition hits allows identification of SG and SG-interacting proteins (Figure 1G). We confirmed that biotinylated proteins are present in SGs (Figures 1H, S1D, and S1I). We identified 256 PABPC1 proximal proteins in fasnall conditions. After subtraction of proteins present in control conditions, 86 proteins remained, 40 of which were overlapping with interactors from arsenite-treated group (Figure 1I and Table S1). Gene ontology of SG-enriched proteins shows a similar pattern of protein distribution, indicating that SGs are similar in all conditions (Figure 1J). Eighteen proteins overlapped with the interactome of another SG component, TDP43 (Freibaum et al., 2010), and two of them were previously identified in the G3BP SG interactome (Markmiller et al., 2018) (Figures 1K, S1J, and S1K).

Fasnall Induces Stress Granules Independent of FASN

Fasnall is a selective FASN inhibitor (Alwarawrah et al., 2016). FASN is a cytoplasmic enzyme essential for *de novo* fatty acid synthesis and can potentially be sequestered in SGs during stress. Interestingly, FASN was proximal to PABPC1 in arsenite conditions (Table S1). First, we looked at FASN localization during SG formation and determined that FASN is not a part of SGs by immunofluorescence microscopy in arsenite and fasnall conditions (Figures 2A and 2B). If SG formation is dependent on the inhibition of FASN, then other small molecules inhibiting the enzyme would be expected to induce SGs as well. We tested another FASN inhibitor, C75, which failed to induce SG formation at a similar concentration (100 μM) (Figures 2C and 2D). To understand the role that FASN inhibition plays in fasnall-induced SG formation we created an FASN

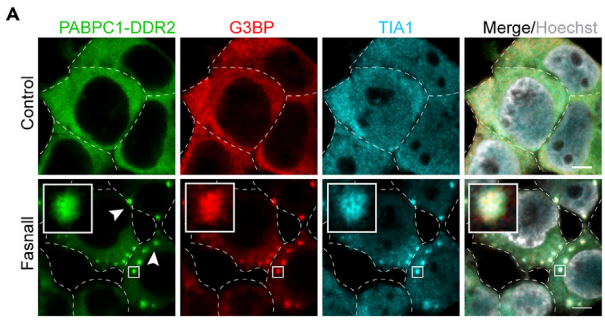

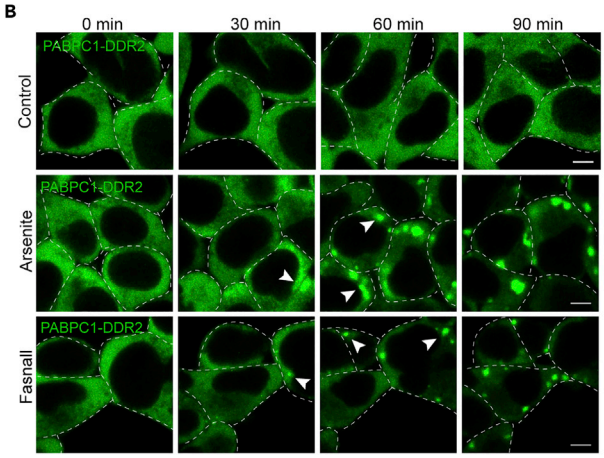

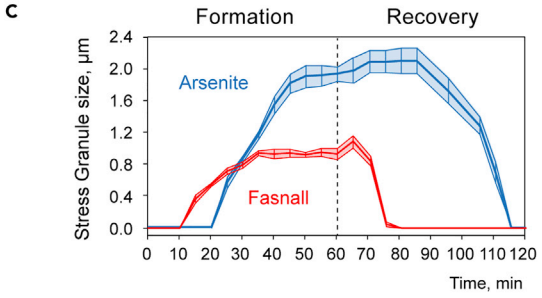

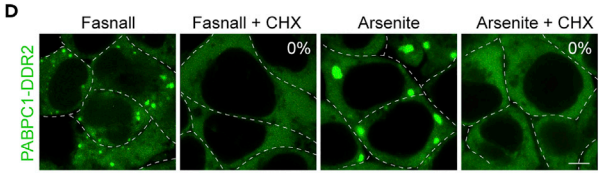

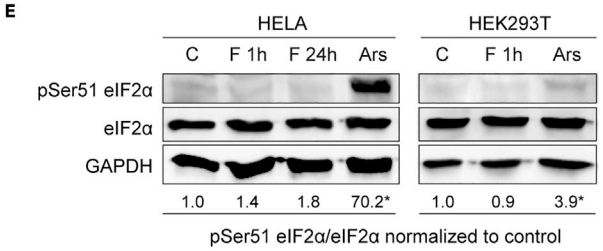

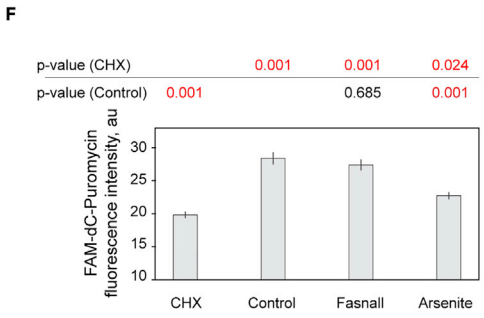

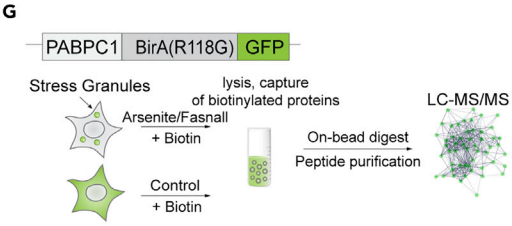

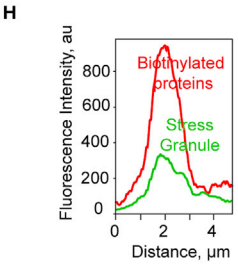

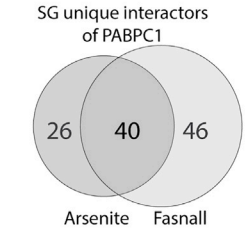

J

	Arsenite	Fasnall
GO: Molecular functon		
RNA binding	59	80
ATP binding	50	50
Ribonucleoprotein complex binding	13	11
Translation regulator activity	12	12
GO: Biological Process		
RNA metabolic process	120	167
Regulation of metabolic process	120	154
Ribonucleoprotein complex biogenesis	52	84
Translation	41	63
GO: Cellular Component		
Intracellular membrane-bounded organelle	178	227
Intracellular non-membrane-bounded organelle	126	176
ribonucleoprotein complex	66	103
Cytoplasmic ribonucleoprotein granule	9	15

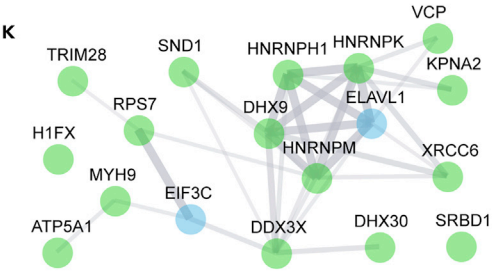

Figure 1. Fasnall Induces Stress Granule Formation

(A) Immunofluorescence of SG markers during fasnall treatment. PABPC1-DDR2 HEK293T cells were treated with fasnall (50 μM) for 1 h. Cells were fixed and stained with anti-TIA1 and anti-G3BP antibodies. Hoechst (10 μg/mL) was used to stain the nucleus 30 min before imaging. Confocal planes are shown; scale bar, 5 μm.

(B) Timeline of SG formation in fasnall and arsenite conditions. HEK293T cells expressing endogenously tagged PABPC1-DDR2 were treated with arsenite (100 μM) or fasnall (50 μM) for indicated amounts of time. Representative confocal images are shown; scale bar, 5 μm. Arrowheads indicate SGs.

(C) Timeline of SG formation and clearance in HEK293T cells expressing PABPC1-DDR2 during fasnall (100 μM) and arsenite (200 μM) treatment for 1 h followed by 1 h of recovery (cells were washed 3 times with the control media). Graph represents average SG size, n = 30. Refer to Figures S1C and S1G.

(D) Confocal microscopy of SG formation in HEK293T cells expressing PABPC1-DDR2 during fasnall (50 μM), fasnall and cycloheximide (10 μg/mL, simultaneous addition), arsenite (100 μM), and arsenite and cycloheximide 1-h treatments; scale bar, 5 μm. (see also Figure S1G for quantification).

(E) Western blot of eIF2 phosphorylation on Ser51 in HELA and HEK293T cell lysates. Cells were treated with fasnall (100 μM, 1 h or 24 h) or arsenite (100 μM, 1 h) before lysis; * - $p<0.01$. (see also Figure S2A for quantification)

(F) Puromycin incorporation assay. Graph shows average fluorescence intensity of FAM-dC-puromycin in the cytoplasm of the HEK293T cells treated with fasnall (100 μM), arsetnie (100 μM), or cycloheximide for 6 h, n = 30; p values relative to control are indicated above the graph.

(G) Schematic of protein identification by liquid chromatography-tandem mass spectrometry. HE293T cells expressing PABPC1 fused to promiscuous biotin ligase BirA (R118G) and GFP were subjected to arsenite or fasnall (100 μM each) with addition of biotin for 6 h after 1 h of treatment. Cells were lysed, and biotinylated proteins were captured on magnetic beads, followed by on-bead digestion and MS.

(H) Fluorescence intensity profile of biotinylated protein enrichment in an SG during fasnall treatment (100 μM). See also Figure S1D for the corresponding images.

(I) Venn diagram of PABPC1 interactors after control subtraction (only hits present in SG conditions and not in control conditions) in different conditions.

(J) Gene ontology (GO) analysis of SG-enriched proteins (hits enriched in SG conditions comparing to control conditions) grouped by conditions. Shown annotations are significantly enriched and hierarchically arranged. Analysis is performed by STRING web tool (https://string-db.org/).

(K) Analysis of SG-enriched fraction by comparison with TDP43-interacting proteins (Freibaum et al., 2010); overlap with the G3BP SG fraction indicated in blue (Markmiller et al., 2017).

knockout using CRISPR/Cas9 (Figures 2E, S1E, and S2B). Interestingly, SG formed to the same extent in the knockout (and hence, independently of FASN availability) (Figures 2F and 2G), indicating that there fasnall exerts additional effects on the cell that are independent of FASN inhibition.

Fasnall-Induced Stress Granules Have Higher Internal Mobility

As noted earlier, fasnall-induced SGs had a markedly different PABPC1 interactome than arsenite-induced SGs. There was, however, another noticeable difference: the majority of fasnall-induced SGs were rounder in shape than arsenite-induced SGs (Figure 3A). To quantify this parameter, we obtained the ratio between the maximal size of the longest (L) side and the side perpendicular to it (S) of single SGs formed in different conditions. Indeed, SGs in fasnall treatment exhibited a ratio closer to 1, indicative of a rounder shape (Figure 3B). SGs have liquid droplet-like properties (Khalfallah et al., 2018; Protter and Parker, 2016; Amen and Kaganovich, 2015), which can be assessed by measuring the internal dynamics of resident proteins. We hypothesized that the rounder shape of fasnall-induced SGs may indicate a more liquid-like state. To measure the internal dynamics of the major SG component PABPC1, which is present in equal concentrations in fasnall- and arsenite-induced SGs (Figures 3C and 3D), we used an endogenously tagged PABPC1-DDR2 cell line. DDR2 is a photoconvertible fluorescent protein, which switches its emission to a longer wavelength upon activation with a non-phototoxic dose of a blue laser (Gurskaya et al., 2006) (Figure 3E). This enables tracking the pool of red (photoconverted) proteins in live cells and in single SGs (Gura Sadovsky et al., 2017) (Figure 3E). We measured the internal dynamics of the largest SGs in the fasnall-induced SG population to reduce size and intensity biases when comparing the diffusion parameter. We photoconverted a small portion of a SG and tracked the red fluorescence intensity until it averaged with the SGs (Figures 3F, fasnall; 3G, arsenite). To account for size differences, we calculated averaging over the same distance that was photoconverted, rather than complete equilibration of the SG. This parameter, which we called diffusion, indicates how fast the photoconverted pool equilibrates with a similar surrounding volume in the SG. Fasnall SGs exhibited faster diffusion than arsenite SGs (Figures 3H and 3I). Together these data indicate that fasnall-induced SGs have readily discernable component and internal dynamic differences from arsenite-induced SGs.

Fasnall Inhibits Growth and Induces Apoptosis

Next, we verified that Fasnall inhibits growth as it was reported previously for different cell lines (Alwarawrah et al., 2016) at a concentration that we used for SG induction (Figures 4A and 4B). Both HEK293T and HeLa cells exhibited a similar decrease in growth compared with control cells (Figures 4A and S1H).

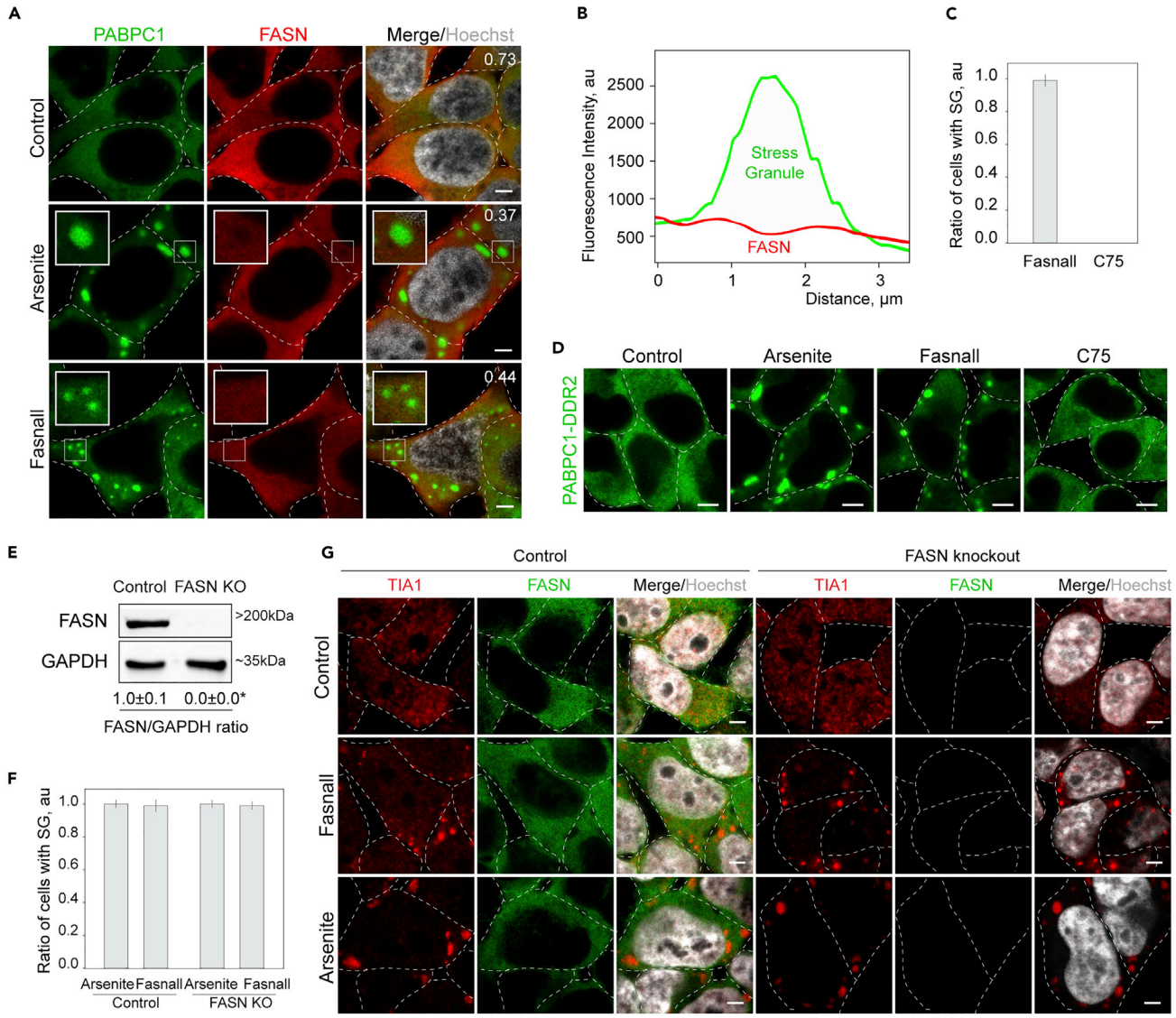

Figure 2. Fasnall Induces SGs Independent of FASN

(A) Immunofluorescence of FASN during SG formation. HEK293T cells expressing endogenously tagged PABPC1-DDR2 were treated with fasnall (50 µM) or arsenite for 1 h. Cells were fixed and stained with anti-FASN antibody. Hoechst (10 µg/mL) was used to stain the nucleus 30 min before imaging. Co-localization coefficient between FASN and PABPC1 is shown in the top right corner of the merged images. Representative confocal planes are shown; scale bar, 5 µm.

(B) Fluorescence intensity profile of FASN and PABPC1 enrichment in an SG during fasnall treatment (100 µM).

(C and D) SG formation in fasnall, C75, and arsenite conditions. HEK293T cells expressing PABPC1-DDR2 were treated with fasnall (50 µM), arsenite (100 µM), and C75 (100 µM) for 1 h. (C) Quantification of the ratio of cells with SGs in the population; mean ± SEM; the ratios (n = 3) were pooled from 300 cells, $p < 0.01$. (D) Representative confocal images are shown; scale bar, 5 µm.

(E) Confirmation of CRISPR/Cas9 knockout (KO) of FASN. Control and FASN KO HEK293T clonal populations were grown to 90% confluency, lysed, and analyzed by western blot. Quantification shows the ratio of FASN to GAPDH. See also Figure S2B.

(F and G) Analysis of Stress Granule formation in control and FASN KO cells. HEK293T WT and FASN KO cells were treated with arsenite (100 µM) or fasnall (50 µM) for 1 h and then fixed and stained with anti-FASN and anti-TIA antibodies (SG marker). (F) Quantification of the ratio of cells with SGs in the population; mean ± SEM, non-significant differences; the ratios (n = 3) were pooled from 300 cells. (G) Representative confocal planes are shown; scale bar, 5 µm.

Fasnall has been shown to induce apoptosis (Alwarawrah et al., 2016), and we confirmed this in the cell lines that we used (Figures 4C and 4D). Additionally we tested growth inhibition in FASN KO cell line and found that fasnall inhibits growth in both control and knockout (Figure 4B).

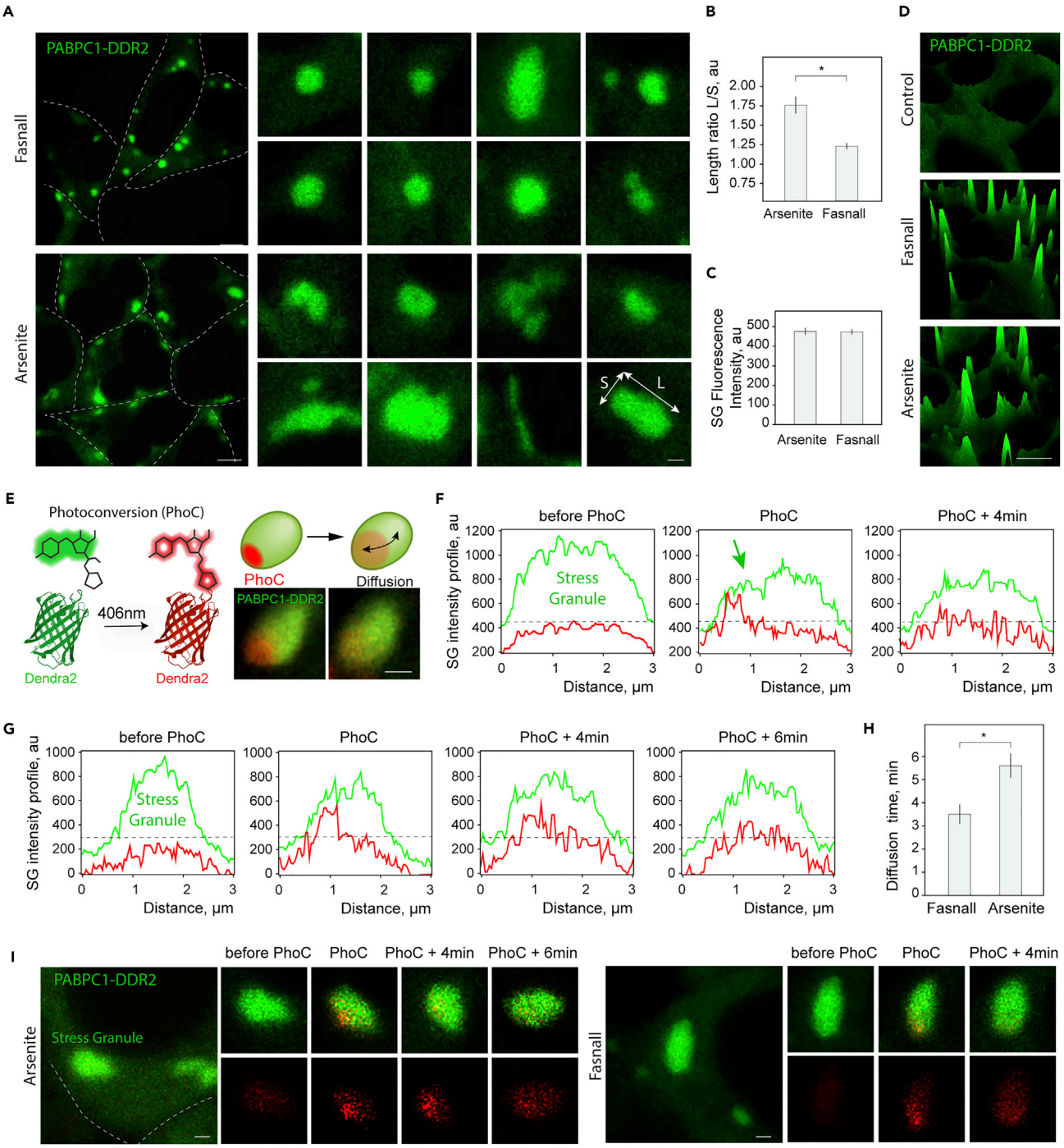

Figure 3. Fasnall-Induced SGs have Higher Internal Mobility

(A and B) Live confocal microscopy of SGs in HEK293T cells expressing endogenously tagged PABPC1-DDR2. Representative confocal planes of single SGs are shown in fasnall and arsenite conditions; scale bar, 1 μm (5 μm for the cells). (B) Quantification shows ratio of maximal length (L) of SGs to a maximal perpendicular width (S); mean ± SEM, n = 25, *p < 0.05.

(C and D) Fluorescence intensity of SGs in HEK293T cells expressing endogenously tagged PABPC1-DDR2. (C) Quantification shows the average intensity of SGs in fasnall and arsenite conditions; mean ± SEM, non-significant difference, n = 100. (D) Intensity surface plot of control and SG conditions; scale bar, 5 μm.

(E) Schematic of photoconversion and example of SG photoconversion using endogenously tagged PABPC1-DDR2 HEK293T cells. Confocal planes show single SGs in live HEK293T cells during and after photoconversion; scale bar, 1 μm.

Figure 3. *Continued*
(F and G) Timeline of the fluorescence intensity profiles of a single SG during photoconversion in fasnall (F) and arsenite (G) conditions. Red graphs represent photoconverted DDR2 population.
(H and I) (H) Quantification of the photoconverted protein diffusion time inside single SGs in fasnall and arsenite conditions; mean ± SEM, n = 15, *p < 0.05. (I) Confocal microscopy of SG photoconversion in HEK293T cells expressing endogenously tagged PABPC1-DDR2 in fasnall and arsenite conditions. Representative confocal planes are shown; scale bar, 1 μm.

DISCUSSION

One of the hallmarks of cancer is the remarkable resilience of cancer cells (Hanahan and Weinberg, 2011). It stems from multifactorial reprogramming, including changes in cellular metabolism, protein synthesis, and stress response pathways (Hanahan and Weinberg, 2011; El-Naggar and Sorensen, 2018). SG formation as a response to chemotherapy appears to be instrumental in providing cancer cells with a platform for signaling and translational control, with an added benefit of protective functions during stress (El-Naggar and Sorensen, 2018). In other cases, however, SGs can exert pro-apoptotic effects (Fujimura et al., 2012; Reineke et al., 2018). We show that the anti-tumor drug, fasnall, induces non-canonical SG formation in different human cell lines at a concentration shown to block cancer cell proliferation and induce apoptosis (Alwarawrah et al., 2016). Although SG formation correlates with apoptosis, it is not clear if SGs exert pro- or anti-apoptotic action, Metabolic reprogramming in cancer often involves reliance on *de novo* fatty acid synthesis by FASN (Rohrig and Schulze, 2016; Koundouros and Poulogiannis, 2020), and inhibition of FASN by fasnall is a promising target in cancer research (Alwarawrah et al., 2016). Here we show that fasnall induces SG formation independently of FASN inhibition. Interestingly, another similar drug, the FASN inhibitor C75 (Kuhajda et al., 2000), does not trigger SG formation in the HEK293T cell line. Fasnall inhibits cancer cell proliferation and induces changes in lipid profiles, and both of these functions are related to FASN inhibition (Alwarawrah et al., 2016). Treatment with 50–100 μM (sufficient to block proliferation) triggers SG formation. It is therefore clear that SGs form not in response to FASN inhibition but to another unknown action of fasnall. Even though SGs may confer stress resilience on cancer cells through their anti-apoptotic function (Gao et al., 2019; Grabocka and Bar-Sagi, 2016), cancer cells with high reliance on protein production cannot easily benefit from a persistent SG response, and SG can have a stalling effect for cellular growth and division. Interestingly, fasnall inhibited growth of both control and FASN KO cells at SG formation concentrations. It is therefore interesting to further explore how SG formation contributes to cell-cycle arrest and to clarify the role of SGs in chemotherapy resistance (Gao et al., 2019).

The internal dynamics of SG and other membraneless compartments are implicated in disease pathology (Mann et al., 2019; Mateju et al., 2017; Patel et al., 2015; Amen and Kaganovich, 2015). Specifically, aberrant aggregation or persistence of SGs can be toxic to cells (Mann et al., 2019). We show that fasnall-induced SGs are different from canonical arsenite-induced SGs in internal dynamics and composition. The shape and liquidity of fasnall-induced SGs can indicate (1) differential association of phase-separating components (Riback, 2020) and (2) lack of external SG interactors that result in a more uniform shape of SGs. For example, a recently identified RNP granule component hnRNPF was enriched in the arsenite-induced SG interactome, but not in fasnall conditions (White et al., 2012). VCP, the regulator of autophagic clearance of SGs was also enriched in arsenite-induced but not fasnall-induced SG interactomes (Buchan et al., 2013) (Figures S1J and S1K). We also found that fasnall-induced SGs have almost four times faster clearance kinetics than those of arsenite-induced SGs, possibly due to reduced size of the fasnall-induced SGs. It is therefore interesting to further explore the differences in clearance mechanisms of fasnall-induced SGs and to investigate the protective functions of SGs in relation to the composition and dynamics of these membraneless compartments.

Limitations of the Study

In this study we found that fasnall induces SG formation. We have not demonstrated, however, if SG formation in case of fasnall plays a causative role in its pro-apoptotic activity in cancer cell lines. We show that SG formation in general correlates with increase in an apoptosis marker. However, whether SGs form to protect the cells or promote apoptosis in these conditions remains to be determined. Our data point toward the unspecific effects when utilizing relatively high concentrations of fasnall, which include SG formation and growth inhibition, and are independent of the inhibitory function of fasnall toward FASN. It would be interesting, therefore, to further examine to what extent the metabolic inhibition of FASN and the unspecific effects contribute to the toxicity.

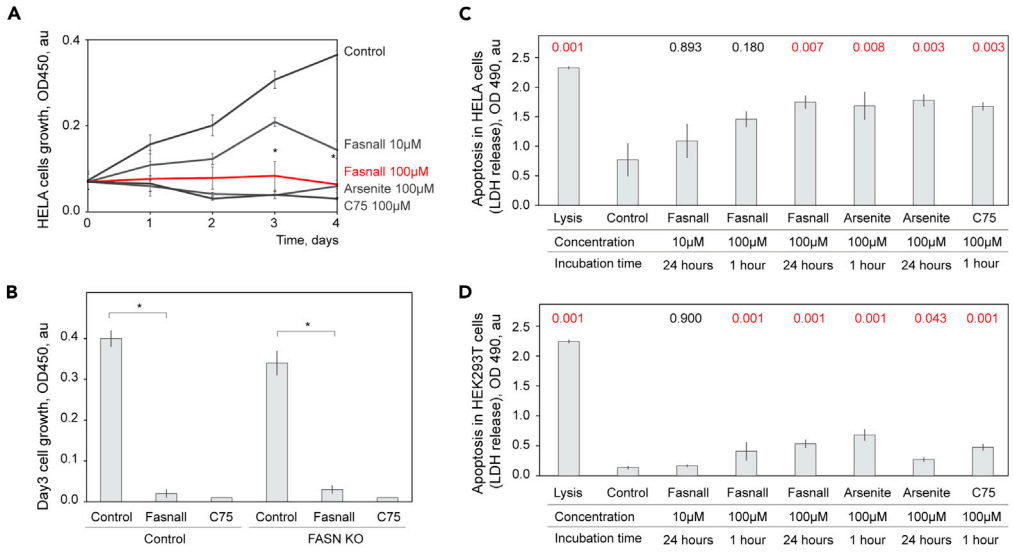

Figure 4. Fasnall Inhibits Cell Growth at SG Inducing Concentrations

(A) Cell growth assessment using WST-8 assay (Cell counting kit-8, Sigma) in HeLa cells grown for 4 days in a complete media supplemented with fasnall, arsenite, or C75 at indicated concentrations; n = 6, *p < 0.05, see also Figure S1H.

(B) Cell growth assessment using WST-8 assay (Cell counting kit-8, Sigma) in HEK293T control and FASN KO cells grown for 3 days in a complete media supplemented with fasnall (100 μM) or C75 (100 μM), n = 6, *p < 0.01.

(C and D) LDH release from HELA (C) or HEK293T (D) cells treated with fasnall, arsenite, C75 for indicated amounts of time; mean ± SEM, n = 6. p Values relative to control are indicated above the graph.

Resource Availability

Lead Contact

Further information and requests for resources and reagents should be directed to and will be fulfilled by the Lead Contact, Daniel Kaganovich, daniel.kaganovich@med.uni-goettingen.de; dan@mail.huji.ac.il.

Materials Availability

Materials generated in this study, e.g. plasmids, will be made available on request.

Data and Code Availability

The mass spectrometry proteomics data have been deposited to the ProteomeXchange Consortium via the PRIDE (Perez-Riverol et al., 2019) partner repository with the dataset identifier PXD021229. Additional data that support the conclusions of this study are available on reasonable request. This study did not generate any code.

METHODS

All methods can be found in the accompanying Transparent Methods supplemental file.

SUPPLEMENTAL INFORMATION

Supplemental Information can be found online at https://doi.org/10.1016/j.isci.2020.101550.

ACKNOWLEDGMENTS

We thank Christof Lenz, Lisa Neuenroth, and Thierry Wasselin at the UMG Core Facility Proteomics for obtaining MS data. William Breuer provided technical assistance with Mass Spectrometry sample preparation. This work was supported by the European Research Council under the European Union's Seventh Framework Program (FP/2007-2013)/ERC-StG2013 337713 DarkSide starting grant. The authors declare no conflicts of interest.

AUTHOR CONTRIBUTIONS

All aspects of the work comprising the manuscript were carried out jointly by D.K. and T.A.

DECLARATION OF INTERESTS

The authors declare no competing interests.

Received: June 8, 2020
Revised: August 23, 2020
Accepted: September 4, 2020
Published: October 23, 2020

REFERENCES

Aditi Mason, A.C., Sharma, M., Dawson, T.R., and Wente, S.R. (2019). MAPK- and glycogen synthase kinase 3-mediated phosphorylation regulates the DEAD-box protein modulator Gle1 for control of stress granule dynamics. J. Biol. Chem. *294*, 559–575.

Adjibade, P., Simoneau, B., Ledoux, N., Gauthier, W.N., Nkurunziza, M., Khandjian, E.W., and Mazroui, R. (2020). Treatment of cancer cells with Lapatinib negatively regulates general translation and induces stress granules formation. PLoS One *15*, e0231894.

Alwarawrah, Y., Hughes, P., Loiselle, D., Carlson, D.A., Darr, D.B., Jordan, J.L., Xiong, J., Hunter, L.M., Dubois, L.G., Thompson, J.W., et al. (2016). Fasnall, a selective FASN inhibitor, shows potent anti-tumor activity in the MMTV-Neu model of HER2(+) breast cancer. Cell Chem. Biol. *23*, 678–688.

Amen, T., and Kaganovich, D. (2015). Dynamic droplets: the role of cytoplasmic inclusions in stress, function, and disease. Cell. Mol. Life Sci. *72*, 401–415.

Amen, T., and Kaganovich, D. (2020). Stress granules sense metabolic stress at the plasma membrane and potentiate recovery by storing active Pkc1. Sci. Signal. *13*, eaaz6339.

Anderson, P., Kedersha, N., and Ivanov, P. (2015). Stress granules, P-bodies and cancer. Biochim. Biophys. Acta *1849*, 861–870.

Arimoto, K., Fukuda, H., Imajoh-Ohmi, S., Saito, H., and Takekawa, M. (2008). Formation of stress granules inhibits apoptosis by suppressing stress-responsive MAPK pathways. Nat. Cell Biol. *10*, 1324–1332.

Aulas, A., Fay, M.M., Lyons, S.M., Achorn, C.A., Kedersha, N., Anderson, P., and Ivanov, P. (2017). Stress-specific differences in assembly and composition of stress granules and related foci. J. Cell Sci. *130*, 927–937.

Bordeleau, M.E., Cencic, R., Lindqvist, L., Oberer, M., Northcote, P., Wagner, G., and Pelletier, J. (2006). RNA-mediated sequestration of the RNA helicase eIF4A by Pateamine A inhibits translation initiation. Chem. Biol. *13*, 1287–1295.

Buchan, J.R., Kolaitis, R.M., Taylor, J.P., and Parker, R. (2013). Eukaryotic stress granules are cleared by autophagy and Cdc48/VCP function. Cell *153*, 1461–1474.

Buchan, J.R., and Parker, R. (2009). Eukaryotic stress granules: the ins and outs of translation. Mol. Cell *36*, 932–941.

Buchan, J.R., Yoon, J.H., and Parker, R. (2011). Stress-specific composition, assembly and kinetics of stress granules in Saccharomyces cerevisiae. J. Cell Sci *124*, 228–239.

Cencic, R., and Pelletier, J. (2016). Hippuristanol - a potent steroid inhibitor of eukaryotic initiation factor 4A. Translation (Austin) *4*, e1137381.

Chen, W.L., Pan, L., Kinghorn, A.D., Swanson, S.M., and Burdette, J.E. (2016). Silvestrol induces early autophagy and apoptosis in human melanoma cells. BMC Cancer *16*, 17.

Choi, S., Sa, M., Cho, N., Kim, K.K., and Park, S.H. (2019). Rbfox2 dissociation from stress granules suppresses cancer progression. Exp. Mol. Med. *51*, 1–12.

Dang, Y., Kedersha, N., Low, W.K., Romo, D., Gorospe, M., Kaufman, R., Anderson, P., and Liu, J.O. (2006). Eukaryotic initiation factor 2alpha-independent pathway of stress granule induction by the natural product pateamine A. J. Biol. Chem. *281*, 32870–32878.

Dewey, C.M., Cenik, B., Sephton, C.F., Johnson, B.A., Herz, J., and Yu, G. (2012). TDP-43 aggregation in neurodegeneration: are stress granules the key? Brain Res. *1462*, 16–25.

El-Naggar, A.M., and Sorensen, P.H. (2018). Translational control of aberrant stress responses as a hallmark of cancer. J. Pathol. *244*, 650–666.

Fournier, M.J., Coudert, L., Mellaoui, S., Adjibade, P., Gareau, C., Cote, M.F., Sonenberg, N., Gaudreault, R.C., and Mazroui, R. (2013). Inactivation of the mTORC1-eukaryotic translation initiation factor 4E pathway alters stress granule formation. Mol. Cell Biol. *33*, 2285–2301.

Fournier, M.J., Gareau, C., and Mazroui, R. (2010). The chemotherapeutic agent bortezomib induces the formation of stress granules. Cancer Cell Int. *10*, 12.

Freibaum, B.D., Chitta, R.K., High, A.A., and Taylor, J.P. (2010). Global analysis of TDP-43 interacting proteins reveals strong association with RNA splicing and translation machinery. J. Proteome Res. *9*, 1104–1120.

Fujimura, K., Sasaki, A.T., and Anderson, P. (2012). Selenite targets eIF4E-binding protein-1 to inhibit translation initiation and induce the assembly of non-canonical stress granules. Nucleic Acids Res. *40*, 8099–8110.

Gao, X., Jiang, L., Gong, Y., Chen, X., Ying, M., Zhu, H., He, Q., Yang, B., and Cao, J. (2019). Stress granule: a promising target for cancer treatment. Br. J. Pharmacol. *176*, 4421–4433.

Grabocka, E., and Bar-Sagi, D. (2016). Mutant KRAS enhances tumor cell fitness by upregulating stress granules. Cell *167*, 1803–1813 e12.

Gura Sadovsky, R., Brielle, S., Kaganovich, D., and England, J.L. (2017). Measurement of rapid protein diffusion in the cytoplasm by photo-converted intensity profile expansion. Cell Rep. *18*, 2795–2806.

Gurskaya, N.G., Verkhusha, V.V., Shcheglov, A.S., Staroverov, D.B., Chepurnykh, T.V., Fradkov, A.F., Lukyanov, S., and Lukyanov, K.A. (2006). Engineering of a monomeric green-to-red photoactivatable fluorescent protein induced by blue light. Nat. Biotechnol. *24*, 461–465.

Hanahan, D., and Weinberg, R.A. (2011). Hallmarks of cancer: the next generation. Cell *144*, 646–674.

Heberle, A.M., Razquin Navas, P., Langelaar-Makkinje, M., Kasack, K., Sadik, A., Faessler, E., Hahn, U., Marx-Stoelting, P., Opitz, C.A., Sers, C., et al. (2019). The PI3K and MAPK/p38 pathways control stress granule assembly in a hierarchical manner. Life Sci. Alliance *2*, e201800257.

Jain, S., Wheeler, J.R., Walters, R.W., Agrawal, A., Barsic, A., and Parker, R. (2016). ATPase-modulated stress granules contain a diverse proteome and substructure. Cell *164*, 487–498.

Jevtov, I., Zacharogianni, M., van Oorschot, M.M., van Zadelhoff, G., Aguilera-Gomez, A., Vuillez, I., Braakman, I., Hafen, E., Stocker, H., and Rabouille, C. (2015). TORC2 mediates the heat stress response in Drosophila by promoting the formation of stress granules. J. Cell Sci. *128*, 2497–2508.

Kaehler, C., Isensee, J., Hucho, T., Lehrach, H., and Krobitsch, S. (2014). 5-Fluorouracil affects assembly of stress granules based on RNA incorporation. Nucleic Acids Res. *42*, 6436–6447.

Kaganovich, D. (2017). There is an inclusion for that: material properties of protein granules provide a platform for building diverse cellular functions. Trends Biochem. Sci. *42*, 765–776.

Kedersha, N., and Anderson, P. (2002). Stress granules: sites of mRNA triage that regulate mRNA stability and translatability. Biochem. Soc. Trans. *30*, 963–969.

Kedersha, N., and Anderson, P. (2007). Mammalian stress granules and processing bodies. Methods Enzymol. *431*, 61–81.

Khalfallah, Y., Kuta, R., Grasmuck, C., Prat, A., Durham, H.D., and vande Velde, C. (2018). TDP-43 regulation of stress granule dynamics in neurodegenerative disease-relevant cell types. Sci. Rep. *8*, 7551.

Kobayashi, T., Winslow, S., Sunesson, L., Hellman, U., and Larsson, C. (2012). PKCalpha binds G3BP2 and regulates stress granule formation following cellular stress. PLoS One *7*, e35820.

Kogure, T., Kinghorn, A.D., Yan, I., Bolon, B., Lucas, D.M., Grever, M.R., and Patel, T. (2013). Therapeutic potential of the translation inhibitor silvestrol in hepatocellular cancer. PLoS One *8*, e76136.

Koundouros, N., and Poulogiannis, G. (2020). Reprogramming of fatty acid metabolism in cancer. Br. J. Cancer *122*, 4–22.

Kuhajda, F.P., Pizer, E.S., Li, J.N., Mani, N.S., Frehywot, G.L., and Townsend, C.A. (2000). Synthesis and antitumor activity of an inhibitor of fatty acid synthase. Proc. Natl. Acad. Sci. U S A *97*, 3450–3454.

Lenzi, J., de Santis, R., de Turris, V., Morlando, M., Laneve, P., Calvo, A., Caliendo, V., Chio, A., Rosa, A., and Bozzoni, I. (2015). ALS mutant FUS proteins are recruited into stress granules in induced pluripotent stem cell-derived motoneurons. Dis. Model. Mech. *8*, 755–766.

Li, Y.R., King, O.D., Shorter, J., and Gitler, A.D. (2013). Stress granules as crucibles of ALS pathogenesis. J. Cell Biol. *201*, 361–372.

Low, W.K., Dang, Y., Schneider-Poetsch, T., Shi, Z., Choi, N.S., Merrick, W.C., Romo, D., and Liu, J.O. (2005). Inhibition of eukaryotic translation initiation by the marine natural product pateamine A. Mol. Cell *20*, 709–722.

Lu, L., Han, A.P., and Chen, J.J. (2001). Translation initiation control by heme-regulated eukaryotic initiation factor 2alpha kinase in erythroid cells under cytoplasmic stresses. Mol. Cell. Biol. *21*, 7971–7980.

Mann, J.R., Gleixner, A.M., Mauna, J.C., Gomes, E., Dechellis-Marks, M.R., Needham, P.G., Copley, K.E., Hurtle, B., Portz, B., Pyles, N.J., et al. (2019). RNA binding antagonizes neurotoxic phase transitions of TDP-43. Neuron *102*, 321–338 e8.

Markmiller, S., Soltanieh, S., Server, K.L., Mak, R., Jin, W., Fang, M.Y., Luo, E.C., Krach, F., Yang, D., Sen, A., et al. (2018). Context-dependent and disease-specific diversity in protein interactions within stress granules. Cell *172*, 590–604 e13.

Mateju, D., Franzmann, T.M., Patel, A., Kopach, A., Boczek, E.E., Maharana, S., Lee, H.O., Carra, S., Hyman, A.A., and Alberti, S. (2017). An aberrant phase transition of stress granules triggered by misfolded protein and prevented by chaperone function. EMBO J. *36*, 1669–1687.

Mazroui, R., Sukarieh, R., Bordeleau, M.E., Kaufman, R.J., Northcote, P., Tanaka, J., Gallouzi, I., and Pelletier, J. (2006). Inhibition of ribosome recruitment induces stress granule formation independently of eukaryotic initiation factor 2alpha phosphorylation. Mol. Biol. Cell *17*, 4212–4219.

Mollet, S., Cougot, N., Wilczynska, A., Dautry, F., Kress, M., Bertrand, E., and Weil, D. (2008). Translationally repressed mRNA transiently cycles through stress granules during stress. Mol. Biol. Cell *19*, 4469–4479.

Patel, A., Lee, H.O., Jawerth, L., Maharana, S., Jahnel, M., Hein, M.Y., Stoynov, S., Mahamid, J., Saha, S., Franzmann, T.M., et al. (2015). A liquid-to-solid phase transition of the ALS protein FUS accelerated by disease mutation. Cell *162*, 1066–1077.

Patton, J.T., Lustberg, M.E., Lozanski, G., Garman, S.L., Towns, W.H., Drohan, C.M., Lehman, A., Zhang, X., Bolon, B., Pan, L., et al. (2015). The translation inhibitor silvestrol exhibits direct anti-tumor activity while preserving innate and adaptive immunity against EBV-driven lymphoproliferative disease. Oncotarget *6*, 2693–2708.

Perez-Riverol, Y., Csordas, A., Bai, J., Bernal-Llinares, M., Hewapathirana, S., Kundu, D.J., Inuganti, A., Griss, J., Mayer, G., Eisenacher, M., et al. (2019). The PRIDE database and related tools and resources in 2019: improving support for quantification data. Nucleic Acids Res. *47*, D442–D450.

Protter, D.S.W., and Parker, R. (2016). Principles and properties of stress granules. Trends Cell Biol. *26*, 668–679.

Rabouw, H.H., Visser, L.J., Passchier, T.C., Langereis, M.A., Liu, F., Giansanti, P., van Vliet, A.L.W., Dekker, J.G., van Der Grein, S.G., Saucedo, J.G., et al. (2020). Inhibition of the integrated stress response by viral proteins that block p-eIF2-eIF2B association. Nat. Microbiol. https://doi.org/10.1038/s41564-020-0759-0.

Reineke, L.C., Cheema, S.A., Dubrulle, J., and Neilson, J.R. (2018). Chronic starvation induces noncanonical pro-death stress granules. J. Cell Sci. *131*, jcs220244.

Riback. (2020). Nature. https://doi.org/10.1038/s41586-020-2256-2.

Rohrig, F., and Schulze, A. (2016). The multifaceted roles of fatty acid synthesis in cancer. Nat. Rev. Cancer *16*, 732–749.

Roux, K.J., Kim, D.I., and Burke, B. (2013). BioID: a screen for protein-protein interactions. Curr. Protoc. Protein Sci. *74*, 19 23 1–19 23 14.

Sfakianos, A.P., Mellor, L.E., Pang, Y.F., Kritsiligkou, P., Needs, H., Abou-Hamdan, H., Desaubry, L., Poulin, G.B., Ashe, M.P., and Whitmarsh, A.J. (2018). The mTOR-S6 kinase pathway promotes stress granule assembly. Cell Death Differ. *25*, 1766–1780.

Slaine, P.D., Kleer, M., Smith, N.K., Khaperskyy, D.A., and Mccormick, C. (2017). Stress granule-inducing eukaryotic translation initiation factor 4A inhibitors block influenza a virus replication. Viruses *9*, 388.

Starck, S.R., Green, H.M., Alberola-Ila, J., and Roberts, R.W. (2004). A general approach to detect protein expression in vivo using fluorescent puromycin conjugates. Chem. Biol. *11*, 999–1008.

Takahara, T., and Maeda, T. (2012). Transient sequestration of TORC1 into stress granules during heat stress. Mol. Cell *47*, 242–252.

Takahashi, M., Higuchi, M., Matsuki, H., Yoshita, M., Ohsawa, T., Oie, M., and Fujii, M. (2013). Stress granules inhibit apoptosis by reducing reactive oxygen species production. Mol. Cell Biol. *33*, 815–829.

Thedieck, K., Holzwarth, B., Prentzell, M.T., Boehlke, C., Klasener, K., Ruf, S., Sonntag, A.G., Maerz, L., Grellscheid, S.N., Kremmer, E., et al. (2013). Inhibition of mTORC1 by astrin and stress granules prevents apoptosis in cancer cells. Cell *154*, 859–874.

Timalsina, S., Arimoto-Matsuzaki, K., Kitamura, M., Xu, X., Wenzhe, Q., Ishigami-Yuasa, M., Kagechika, H., and Hata, Y. (2018). Chemical compounds that suppress hypoxia-induced stress granule formation enhance cancer drug sensitivity of human cervical cancer HeLa cells. J. Biochem. *164*, 381–391.

Walker, A.K., Soo, K.Y., Sundaramoorthy, V., Parakh, S., Ma, Y., Farg, M.A., Wallace, R.H., Crouch, P.J., Turner, B.J., Horne, M.K., and Atkin, J.D. (2013). ALS-associated TDP-43 induces endoplasmic reticulum stress, which drives cytoplasmic TDP-43 accumulation and stress granule formation. PLoS One *8*, e81170.

Wheeler, J.R., Matheny, T., Jain, S., Abrisch, R., and Parker, R. (2016). Distinct stages in stress granule assembly and disassembly. Elife *5*, e18413.

White, R., Gonsior, C., Bauer, N.M., Kramer-Albers, E.M., Luhmann, H.J., and Trotter, J. (2012). Heterogeneous nuclear ribonucleoprotein (hnRNP) F is a novel component of oligodendroglial RNA transport granules contributing to regulation of myelin basic protein (MBP) synthesis. J. Biol. Chem. *287*, 1742–1754.

Wolozin, B., and Ivanov, P. (2019). Stress granules and neurodegeneration. Nat. Rev. Neurosci. *20*, 649–666.

Zhang, K., Daigle, J.G., Cunningham, K.M., Coyne, A.N., Ruan, K., Grima, J.C., Bowen, K.E., Wadhwa, H., Yang, P., Rigo, F., et al. (2018). Stress granule assembly disrupts nucleocytoplasmic transport. Cell *173*, 958–971 e17.

iScience, Volume *23*

Supplemental Information

Fasnall Induces Atypically Transient Stress Granules Independently of FASN Inhibition

Triana Amen and Daniel Kaganovich

Figure S1

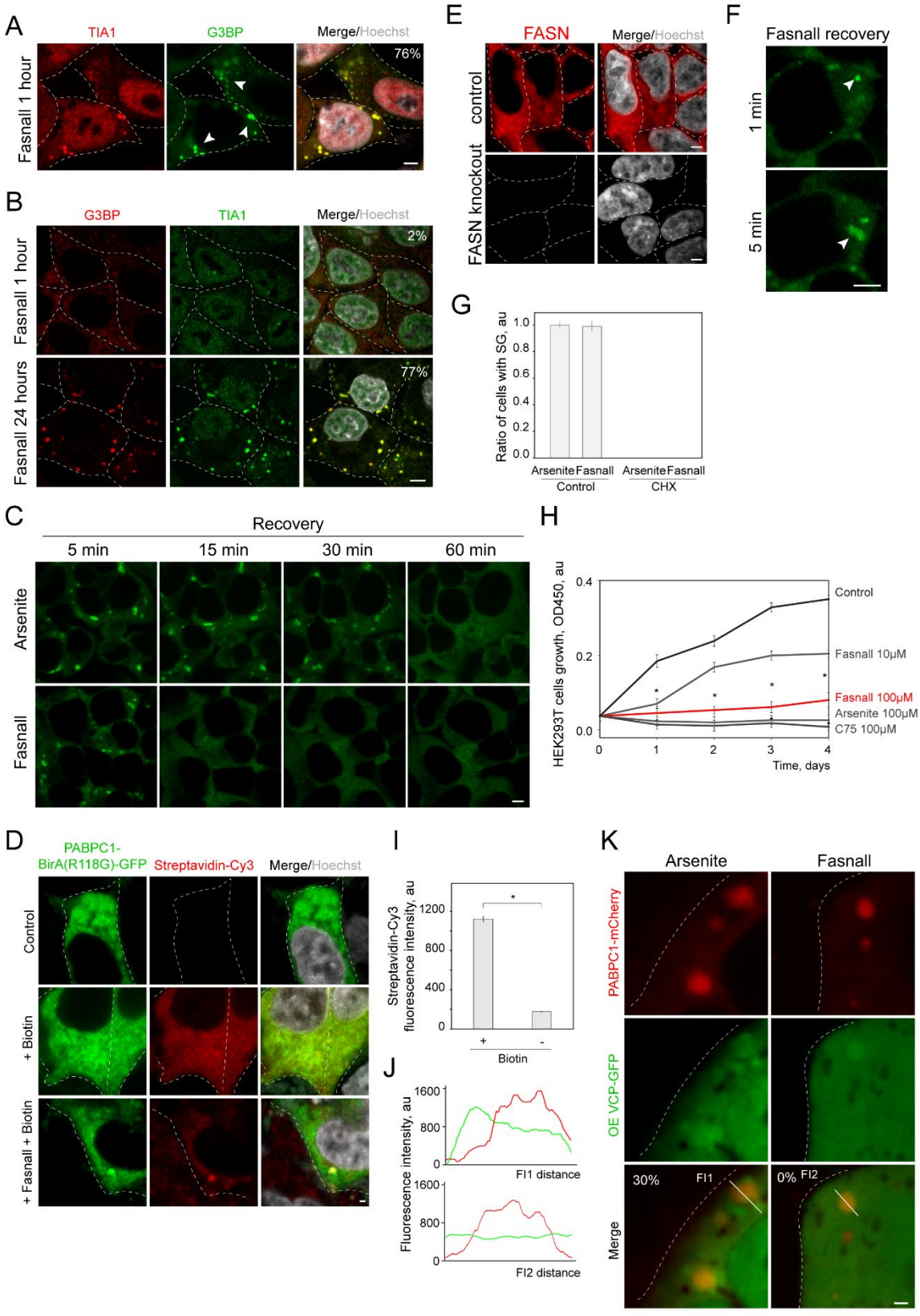
A
TIA1
G3BP
Merge/Hoechst
Fasnall 1 hour
76%
B
G3BP
TIA1
Merge/Hoechst
Fasnall 1 hour
2%
Fasnall 24 hours
77%
E
FASN
Merge/Hoechst
control
FASN knockout
F
Fasnall recovery
1 min
5 min
G
Ratio of cells with SG, au
1.0
0.8
0.6
0.4
0.2
0.0
Arsenite
Fasnall
Arsenite
Fasnall
Control
CHX
C
Recovery
5 min
15 min
30 min
60 min
Arsenite
Fasnall
H
HEK293T cells growth, OD450, au
0.4
0.2
0.0
0
1
2
3
4
Time, days
Control
Fasnall 10μM
Fasnall 100μM
Arsenite 100μM
C75 100μM
D
PABPC1-
BirA(R118G)-GFP
Streptavidin-Cy3
Merge/Hoechst
Control
+ Biotin
+ Fasnall + Biotin
I
Streptavidin-Cy3
fluorescence intensity, au
1200
800
400
0
+
-
Biotin
J
Fluorescence intensity, au
1600
800
0
FI1 distance
1600
800
0
FI2 distance
K
Arsenite
Fasnall
PABPC1-mCherry
OE VCP-GFP
Merge
30%
FI1
0%
FI2

Figure S1. Related to Figures 1, 2, and 4.

(A) SG formation in SHSY-5Y cells. Cells were treated with fasnall (100μM) for 1 hour and fixed. Stress Granules marker (G3BP and TIA1) were visualized using immunostaining. Representative confocal planes are shown, arrowheads indicate SGs, scale bar 5μm. Number in the top right corner indicates percentage of cells with SGs in the population.

(B) SG formation in HeLa cells treated with fasnall (100μM) for indicated amounts of times. Stress Granules marker (G3BP and TIA1) were visualized using immunostaining. Representative confocal planes are shown, arrowheads indicate SGs, scale bar 5μm. Numebr in the top right corner indicates percentage of cells with SGs in the population.

(C) Timeline of SG clearance in fasnall and arsenite conditions. HEK293T cells expressing endogenously tagged PABPC1-DDR2 were treated with arsenite (200 μM) or fasnall (100 μM) for 1 hour and washed 3 times with the control media. Representative confocal images are shown, scale bar 5μm.

(D, I) Visualization of protein biotinylation during Stress Granule formation. Cells expressing PABPC1-BirA(R118G)-GFP were treated with fasnall (100μM) for 1 hour following addition of biotin (100μM) for 4 hours. (D) Cells were fixed in PFA and stained with streptavidin-Cy3. Confocal planes are shown, scale bar 1μm. (I) Quantification shows enrichment of biotinylated proteins upon biotin addition, mean± SEM, n=25, * - $p<0.01$.

(E) Verification of FASN knockout with immunofluorescence. HEK293T cells were grown to 90% confluency fixed and FASN was visualized. Hoechst (10μg/ml) was used to stain the nucleus 30 minutes prior to imaging. Representative confocal images are shown, scale bar 5μm.

(F) Timeline of SG clearance in fasnall conditions. HEK293T cells expressing endogenously tagged PABPC1-DDR2 were treated with fasnall (100 μM) for 1 hour and washed 3 times with the control media. Representative confocal images of the same cell are shown, scale bar 5μm. Arrowheads indicate SGs.

(G) Quantification of Stress Granule formation in fasnall and arsenite conditions in control and cycloheximide addition, mean± SEM, n=3 ratios pooled from 300 cells.

(H) Cell growth assessment using WST-8 assay (Cell counting kit-8, Sigma) in HEK293T cells grown for 4 days in a complete media supplemented with Fasnall, Arsenite, or C75 at an indicated concentrations, n=6, * - $p<0.05$

(J-K) Confocal microscopy of SGs in cells overexpressing GFP tagged VCP, and endogenously tagged PABPC1-mCherry were treated with fasnall (100μM) or arsenite (100μM) for 1 hour, representative confocal images (K) and corresponding intensity profiles (J) are shown, scale bar 5μm.

Figure S2

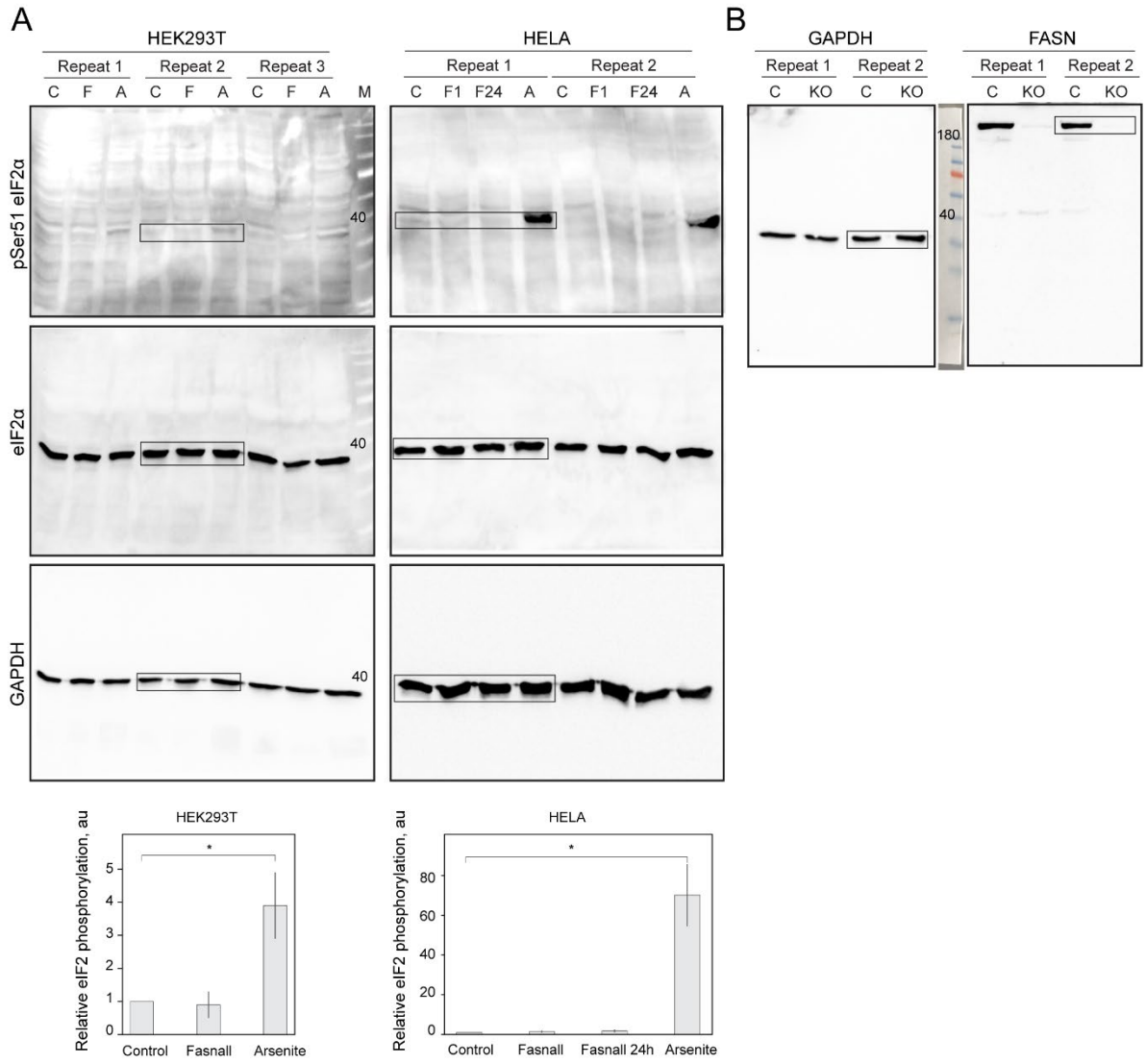

Figure S2. Related to Figures 1 and 2.
(A) Western blot of eIF2α phosphorylation on Ser51 in HeLa and HEK293T cell lysates. Cells were treated with fasnall (100 μM, 1 hour or 24 hours), or arsenite (100 μM, 1hour) before lysis. **(B)** Confirmation of CRISPR/Cas9 knockout (KO) of FASN. Control and FASN KO HEK293T clonal population were grown to 90% confluency, lysed, and analyzed by western blot.

Transparent Methods

Cell culture and cell lines

HEK293T cells were maintained in DMEM supplemented with 10% fetal bovine serum (FBS), 1% penicillin/streptomycin, at 37°C/5% CO2, SH-SY5Y cells were maintained in 1:1 F12/DMEM media supplemented with 10% fetal bovine serum (FBS), 1% penicillin/streptomycin at 37°C/5% CO2. Cells modified via CRISPR/Cas9 were maintained as above with addition of puromycin (2μg/ml, Sigma) during selection of clonal populations.

Antibodies

We used the following reagents to detect proteins: monoclonal anti-G3BP (Sigma-Aldrich WH0010146M1), polyclonal anti-TIA1 produced in rabbit (Sigma-Aldrich SAB4301803), anti-GAPDH (sc-47724, Santa Cruz Biotechnology), anti-FASN (Sigma, SAB1403807).

Secondary antibodies for immunofluorescence: anti-Rabbit IgG Cy3-conjugated (Sigma-Aldrich C2306), anti-Mouse IgG Cy3-conjugated (Sigma-Aldrich C2181), anti-rabbit IgG Cy5 conjugated (Invitrogen A10523), eIF2α (9722, Cell Signaling Technology), Phospho-eIF2α (Ser51) (9721, Cell Signaling Technology).

Chemicals

Hoechst (Sigma), sodium arsenite (Fischer Chemical), cycloheximide (Sigma), Streptavidin-Cy3 (Thermo Fischer Scientific), Streptavidin-HRP (Thermo Scientific), fatty acid free BSA (PAN Biotech), DMEM (PAN Biotech), FBS (PAN Biotech), PBS (PAN Biotech), methanol (Roth), Chlorophorm (Sigma), biotin (Sigma), aprotinin (Roth), leupeptin (Roth), Phenylmethylsulfonyl fluoride (PMSF, Sigma), fasnall (Sigma), C75 (Sigma), FAM-dC-Puromycin (Jena Bioscience).

Growth and apoptosis assessment.

Cell growth was calculated using Cell counting kit-8 (Sigma). LDH release was calculated using (Cytotoxicity Detection KitPLUS (LDH), Sigma).

CRISPR/Cas9

Knockout and endogenously tagged cell lines were constructed using CRISPR/Cas9 protocol and plasmids described in Ran et. al (Ran et al., 2013). Knockout cell lines were verified by western blotting, immunofluorescence. Genomic DNA was sequenced to verify disrupted region in knockout or fidelity of endogenous tagging. CRISPR specificity was profiled using Digenome-Seq web tool (http://www.rgenome.net/cas-offinder/) (Bae et al., 2014). Off targets were not found. The following target sequences are used to modify genomic DNA: knockout of FASN – GAAGCTGCCAGAGTCGGAGAACTTGC.

Plasmid Construction:

All plasmids were constructed using Escherichia coli strain DH5α. Plasmids used in this study are summarized in the Table 1. We used px459 plasmid to clone CRISPR/Cas9 constructs for gene knockout. pSpCas9(BB)-2A-Puro (PX459) V2.0 was a gift from Feng Zhang (Addgene plasmid # 62988 ; http://n2t.net/addgene:62988 ; RRID:Addgene_62988) (Ran et al., 2013). pEGFP-C1-VCP plasmid was a gift from Dr. Akira Kakizuka.

Plasmid name	Source
Px330-FASN-KO-gRNA	This study
pcDNA-PABPC1-BirA(R118G)-GFP	Amen and Kaganovich, in review

Extraction of biotinylated proteins

Cells expressing PABPC1-BirA(R118G)-GFP were grown to 80-90% confluency. SGs were induced with 100 μM arsenite, or fasnall. After 1 hour, cells were incubated with biotin (100μM) for 6 hours, SGs formation was visualized on the microscope. Lysis and affinity capture was done according to Roux et al. with minor modifications (Roux et al., 2012). Cells were washed with PBS

and (subsequent steps at 4°C) lysed in the buffer (50mM Tris pH7.4, 500mM NaCl, 0.4%SDS, 5mM EDTA, 1mM DTT, and protease inhibitor cocktail (aprotinin, leupeptin, and PMSF, 10µg) with glass beads 425-600 µm (Sigma). After 1min of vortex Triton X-100 was added to 2% concentration, after second round of vortex equal amount of 50mM Tris pH7.4 was added. After third round of vortex and centrifugation 5min 13000 rpm 300µl of streptavidin-coated magnetic beads (NEB) were added to collected supernatants and incubated overnight at 4°C with agitation, 10% of the sample was collected for the Western Blot analysis. Beads were collected and (subsequent steps at room temperature) washed according to Roux et al.

Preparing samples for the Mass spectroscopy

The beads were washed free of detergents by two washes with 25 mM Tris-HCl pH 8.0. Then the packed beads were resuspended in 100 ul of 8M urea, 10 mM DTT, 25 mM Tris-HCl pH 8.0 and incubated for 20 min, followed by addition of iodoacetamide to a concentration of 55 mM and incubation for 20 min in the dark. The urea was diluted by the addition of 6 volumes of 25 mM Tris-HCl pH 8.0, 0.25 µg trypsin was added (Sigma) and the beads were incubated overnight at 37ºC with gentle agitation. The released peptides were desalted by loading the whole bead supernatant on C18 Stage tips (Rappsilber et al., 2007). Eluted peptide material was used for MS analysis.

Measurement of active translation

Cells were incubated with 0.5µM 6-FAM-dC-Puromycin (FAM-dC-Puro, Jena Bioscience) for 6 hours, fluorescence intensity was measured in the cytoplasm of single cells (n=30), in the indicated conditions. Incorporation of puromycin was considered a readout of active translation according to (Starck et al., 2004).

LC/MS/MS analysis

Protein digests were analyzed on a nanoflow chromatography system (Eksigent nanoLC425) hyphenated to a hybrid triple quadrupole-TOF mass spectrometer (TripleTOF 5600+) equipped with a Nanospray III ion source (Ionspray Voltage 2400 V, Interface Heater Temperature 150°C, Sheath Gas Setting 12) and controlled by Analyst TF 1.7.1 software build 1163 (all AB Sciex). In brief, peptides were dissolved in loading buffer (2% acetonitrile, 0.1% formic acid in water), enriched on a precolumn (0.18 mm ID x 20 mm, Symmetry C18, 5 µm, Waters, Milford/MA, U.S.A) and separated on an analytical RP-C18 column (0.075 mm ID x 250 mm, HSS T3, 1.8 µm, Waters) using a 90 min linear gradient of 5-35 % acetonitrile/0.1% formic acid (v:v) at 300 nl min^{-1}.

Qualitative LC/MS/MS analysis was performed using a Top25 data-dependent acquisition method with an MS survey scan of m/z 350–1250 accumulated for 350 ms at a resolution of 30,000 full width at half maximum (FWHM). MS/MS scans of m/z 180–1600 were accumulated for 100 ms at a resolution of 17,500 FWHM and a precursor isolation width of 0.7 FWHM, resulting in a total cycle time of 2.9 s. Precursors above a threshold MS intensity of 125 cps with charge states 2+, 3+, and 4+ were selected for MS/MS, the dynamic exclusion time was set to 30 s. MS/MS activation was achieved by CID using nitrogen as a collision gas and the manufacturer's default rolling collision energy settings. Two technical replicates per sample were acquired.

MS data analysis

Mass spectra data were processed using the MaxQuant computational platform, version 1.6.3.4 (Cox and Mann, 2008). Peak lists were searched against the human Uniprot FASTA sequence database (downloaded 02.01.19). The search included cysteine carbamidomethylation as a fixed modification and oxidation of methionine as variable modifications. Peptides with minimum of seven amino-acid length were considered and the required FDR was set to 1% at the peptide and protein level. Protein identifications required at least three unique or razor peptides per protein group. Relative protein quantification in MaxQuant was performed using the label free

quantification (LFQ) algorithm (Cox et al., 2014). Identified proteins were analyzed with Perseus software (Tyanova et al., 2016). Gene ontology analysis was performed using STRING web tool (https://string-db.org/,(Szklarczyk et al., 2015).

Microscopy

For live cell imaging we used 4-well microscope glass bottom plates (IBIDI), or Cellview cell culture dish (Greiner Bio One). Plates were coated with Concanavalin A (Sigma) for live cell imaging of yeast. Confocal images and movies were acquired using a dual point-scanning Nikon A1R-si microscope equipped with a PInano Piezo stage (MCL), temperature and CO2 incubator, using a 60x PlanApo VC oil objective NA 1.40. We used 406nm, 488nm, 561nm, and 640nm laser (Coherent, OBIS). Movies for kymographs were acquired in resonant-scanning mode. Image processing was performed using NIS-Elements software.

Statistics and data analysis

Three or more independent experiments were performed to obtain the data. P values were calculated by two-tailed Student t-test, or one-way ANOVA for samples following normal distribution. Normal distribution of the data was verified using Shapiro-Wilk test and the equality of variances was verified by Levene's test. Mann-Whitney, or Kruskal-Wallis tests were used for experiments with less than 5 samples or when samples didn't follow a normal distribution. The sample sizes were not predetermined. Scatter plots were generated using Matplotlib (Hunter, 2007).

Supplemental References

BAE, S., PARK, J. & KIM, J. S. 2014. Cas-OFFinder: a fast and versatile algorithm that searches for potential off-target sites of Cas9 RNA-guided endonucleases. *Bioinformatics,* 30**,** 1473-5.

COX, J., HEIN, M. Y., LUBER, C. A., PARON, I., NAGARAJ, N. & MANN, M. 2014. Accurate proteome-wide label-free quantification by delayed normalization and maximal peptide ratio extraction, termed MaxLFQ. *Molecular & Cellular Proteomics,* 13**,** 2513-26.

COX, J. & MANN, M. 2008. MaxQuant enables high peptide identification rates, individualized p.p.b.-range mass accuracies and proteome-wide protein quantification. *Nat Biotechnol,* 26**,** 1367-72.

HUNTER, J. D. 2007. Matplotlib: A 2D graphics environment. *Computing in Science & Engineering,* 9**,** 90-95.

RAN, F. A., HSU, P. D., WRIGHT, J., AGARWALA, V., SCOTT, D. A. & ZHANG, F. 2013. Genome engineering using the CRISPR-Cas9 system. *Nat Protoc,* 8**,** 2281-2308.

RAPPSILBER, J., MANN, M. & ISHIHAMA, Y. 2007. Protocol for micro-purification, enrichment, pre-fractionation and storage of peptides for proteomics using StageTips. *Nat Protoc,* 2**,** 1896-906.

ROUX, K. J., KIM, D. I., RAIDA, M. & BURKE, B. 2012. A promiscuous biotin ligase fusion protein identifies proximal and interacting proteins in mammalian cells. *J Cell Biol,* 196**,** 801-10.

STARCK, S. R., GREEN, H. M., ALBEROLA-ILA, J. & ROBERTS, R. W. 2004. A general approach to detect protein expression in vivo using fluorescent puromycin conjugates. *Chem Biol,* 11**,** 999-1008.

SZKLARCZYK, D., FRANCESCHINI, A., WYDER, S., FORSLUND, K., HELLER, D., HUERTA-CEPAS, J., SIMONOVIC, M., ROTH, A., SANTOS, A., TSAFOU, K. P., KUHN, M., BORK, P., JENSEN, L. J. & VON MERING, C. 2015. STRING v10: protein-protein interaction networks, integrated over the tree of life. *Nucleic Acids Res,* 43**,** D447-52.

TYANOVA, S., TEMU, T., SINITCYN, P., CARLSON, A., HEIN, M. Y., GEIGER, T., MANN, M. & COX, J. 2016. The Perseus computational platform for comprehensive analysis of (prote)omics data. *Nat Methods,* 13**,** 731-40.